Check for updates

Carbon Energy

WILEY

CARBON ENERGY

RESEARCH ARTICLE OPEN ACCESS

Durable Fuel Cell Cathode Enabled by Pt Embedded Nanoscale Carbon Network via a Scalable Process

Suriya Venkatesan[1,2] | Jens Mitzel[1] | Tobias Morawietz[1] | Emmanuelle Boehm-Courjault[3] | Deven P. Estes[4] | Laure Guétaz[5] | Indro Biswas[1] | Jan Van Herle[3] | Karsten Wegner[6] | Pawel Gazdzicki[1] | Kaspar Andreas Friedrich[1,2]

[1]Department of Electrochemical Energy Technology, Institute of Engineering Thermodynamics, German Aerospace Center (DLR), Stuttgart, Baden-Württemberg, Germany | [2]Institute of Building Energetics, Thermal Engineering and Energy Storage (IGTE), University of Stuttgart, Stuttgart, Baden-Württemberg, Germany | [3]Group of Energy Materials, École Polytechnique Fédérale de Lausanne, Sion, Valais, Switzerland | [4]Institute of Technical Chemistry, University of Stuttgart, Stuttgart, Baden-Württemberg, Germany | [5]University of Grenoble Alpes, CEA, LITEN, Grenoble, Auvergne-Rhône-Alpes, France | [6]ParteQ GmbH, Malsch, Baden-Württemberg, Germany

Correspondence: Pawel Gazdzicki (Pawel.Gazdzicki@dlr.de)

Received: 6 February 2026 | **Revised:** 5 May 2026 | **Accepted:** 13 May 2026

Funding: SUSTAINCELL, Grant/Award Number: 101101479; Clean Hydrogen Partnership; Hydrogen Europe; Hydrogen Europe Research

ABSTRACT

Proton exchange membrane fuel cells (PEMFC) suffer significant voltage degradation at lower Pt loadings on the cathode. Expedited commercialization and sustainable utilization of scarce resources demand highly durable Pt-based electrocatalysts produced via rapid, scalable processes. We present Pt nanoparticles (≈ 2 nm) embedded in a nanoscale carbon network, produced via controlled-atmosphere flame spray pyrolysis, where native Pt nuclei serve as structural guides for the nanoscale overlayer. The gas-phase-derived porous catalyst exhibits high accessibility to Pt and uncompromised oxygen reduction activity upon activation and demonstrates at least fourfold lower performance loss at high current densities and fivefold lower electrochemical active surface area loss compared to state-of-the-art alternatives in low-Pt-content fuel cells. The strong interfacial coordination between Pt and its surface-grown carbon network, combined with the continuous, favorable structural evolution of the catalyst and catalyst layer, remarkably suppresses Pt degradation mechanisms, including ionomer poisoning and Pt dissolution, facilitates H^+ and O_2 transport to the catalyst, and ensures sustained performance under harsh fuel cell operating conditions.

1 | Introduction

Decarbonizing the mobility sectors and achieving net-zero emissions by 2050 deeply relies on sustainable nanostructured catalysts and overcoming the entangled challenges in cost and durability. The development of finely dispersed precious metal catalyst nanostructures with tunable composition, catalyst nanoparticle size, surface area, and surface protection in a cost-effective, highly scalable one-step process may accelerate the engineering of catalysts with enhanced durability for harsh reaction conditions, such as the kinetically slow oxygen reduction reaction (ORR) in fuel cells and batteries [1, 2]. Particularly, in light of large-scale green hydrogen deployment potential in proton exchange membrane fuel cells (PEMFC), which offer high-power density and quick start-up [3], ensuring the durability of electrocatalysts becomes crucial. This includes lifetimes of up to 30,000 h for heavy-duty vehicles, trains, aviation, and stationary applications, and up to 80,000 h for maritime applications [4]. However, the durability of a fuel cell cathode suffers from structural and catalytic instability of electrocatalysts, caused by phenomena such as coalescence, aggregation, Oswald ripening, corrosion, and ionomer poisoning during ORR [1, 5]. Therefore, maintaining performance presently depends on high loading of platinum group metals

This is an open access article under the terms of the Creative Commons Attribution License, which permits use, distribution and reproduction in any medium, provided the original work is properly cited.

© 2026 The Author(s). *Carbon Energy* published by Wenzhou University and John Wiley & Sons Australia, Ltd.

(PGM), which account for 54% of the stack cost for large-scale production [6]. Although efforts such as controlled catalyst nanostructures through doping, alloying, intermetallizing with, or PGM coating on abundantly available transition metals show enhanced activity, despite the scale-up challenges, the aforementioned catalytic degradation processes persist at temperatures ≥ 80°C [5, 7, 8].

Thus, confining catalyst nanoparticles (NPs) with enhanced catalytic properties requires additional morphological barriers [7], such as preformed mesoporous carbon structures, metal organic frameworks, zeolite nanocages, and oxide/carbon-based encapsulating layers [9]. One promising and commercially scaled-up catalyst involves annealed high surface area carbon (C_{HSA})-supported PGM catalysts (e.g., Pt, PtRu, or PtCo on C_{HSA}) [10, 11], where a fraction of catalyst NPs reside inside open mesopores and remain accessible to reactant molecules [11]. Despite demonstrating reduction in catalyst degradation and resistance to CO and SO_x poisoning [12, 13], the long-term durability of PEMFC utilizing these catalysts remains insufficient at PGM loadings below 0.2 mg cm^{-2} or 0.25 g kW^{-1} at 0.65 V—the EU Clean Hydrogen Joint Undertaking (CH-JU) target for 2030 [14]. This is because neighboring PGM NPs, both inside and outside mesopores, are still prone to degradation. While depositing an additional thin carbon layer (≈ 1 nm) to encapsulate Pt residing on the carbon surface could be a favorable countermeasure to block Pt movement [15], proper design of the encapsulation is critical. The design should ensure a less adsorptive and more O_2-permeable interface [5, 8], as well as resistance to electrochemical corrosion. Additionally, strategies such as embedding Pt NPs into preformed carbon and the in-situ growth of Pt with nanocages—either forming small Pt clusters that are strongly adsorptive to oxygen intermediates [16] or aggregates on frameworks [9]—lower electrochemical dissolution potentials. Nevertheless, current and primary wet-chemical and solid-state synthesis approaches for such multi-component catalyst assemblies involve numerous delicate, time-consuming, and energy-intensive steps [1, 5, 7–9, 11, 16], limiting economically viable scale-up prospects. In methods that separate support, catalyst, and encapsulating layer synthesis, suppressed interactions between components can alter the intrinsic properties of metal entities.

Therefore, developing protected porous catalyst nanostructures utilizing highly scalable single-step gas-phase production techniques, such as flame spray pyrolysis (FSP) [17–20], could offer unprecedented prospects. Researchers have recently developed interesting material structures [18, 21–23] for various applications using this technology. FSP techniques are employed industrially for the large-scale (ton h^{-1}) continuous production of carbon black. Integrating PGM or other metal or alloy catalysts directly with carbon structure production in one continuous process could provide substantial economic advantages over conventional synthesis routes. However, to the best of our knowledge, Ernst et al. [24] were the only researchers to report carbon-embedded Pt NPs with only 2.6 wt.% Pt using FSP or similar flame aerosol techniques in one-step, although their further exploration was discontinued due to initial inactivity of the catalyst toward the hydrogenation of cyclohexene and inhomogeneous Pt dispersion (see Supporting Information S1: Table S1 for detailed literature comparison). Further discussions on FSP fundamentals, versatility, scalability from lab to industry, economic viability, and advantages over conventional batch-type wet- and dry-chemical routes can be found in references [17, 25–27]. In this study, as an example, we present a functional and homogeneous electrocatalyst consisting of Pt NPs (≈ 30 wt. %) embedded in a nanoscale carbon network (denoted as Pt-e-Cn) prepared using FSP techniques in laboratory scale (Figure 1). Using the ORR as a model reaction, we demonstrate its high activity and excellent durability after proper catalyst activation in a practical PEMFC cathode. Through a combination of electrochemical and microscopy tools, the strong impact of the nanocomposite on the catalytic durability is highlighted.

2 | Results and Discussion

2.1 | Controlled Synthesis and Structure Evaluation of Pt-e-Cn

Pt-e-Cn with (30 ± 2) wt.% Pt was prepared by FSP techniques (Figure 2 and Supporting Information S1: Figure S1), with a precursor solution containing platinum acetylacetonate ($Pt(O_2C_5H_7)_2$) dissolved in xylenes ($C_6H_4(CH_3)_2$, the primary carbon source) and dispersed with oxygen in a nitrogen co-flow. The atomized precursor droplets were ignited by a support flame, forming the main spray flame—the reactor—where the majority of the total enthalpy is provided by the precursor itself. Combustion of droplets and decomposition of precursor lead to near atomic-scale dispersion of Pt species in the flame atmosphere (Supporting Information S1: Figure S2). Condensed Pt nuclei typically evolve from the gas-phase and then grow by collision-sintering and/or condensation, forming Pt clusters and crystalline NPs within milliseconds in the hot zone, where the temperature reaches up to 3000 K [18]. The Pt surfaces are catalytically active toward the combustion of carbonaceous compounds, and increasing the Pt content in the precursor accelerates hydrocarbon consumption in the flame atmosphere. While consuming available oxygen in the controlled oxygen-lean atmosphere, the Pt clusters and NPs likely act as nuclei for the growth of thin carbon layers through hydrocarbon decomposition on their surface (Supporting Information S1: Figure S2), enabling the formation of Pt-embedded carbon [24]. As carbon grows, Pt growth is suppressed, while neighboring carbon-coated nanoparticles continue to grow by surface reaction or agglomeration, forming a randomly interconnected carbon nanoscale network with embedded-Pt NPs (Pt-e-Cn; Figure 2A–C and Supporting Information S1: Figure S2B,C). The process is followed by abrupt N_2 quenching at 300 mm above the atomizer, which terminates further chemical reactions downstream of the flame, reaching only ≈ 400 K at the Pt-e-Cn collection filter. It is important to note that, unlike in the study of Ernst et al. [24], the use of an optimized oxygen-lean reaction zone length (i.e., 300 mm tube enclosure), followed by rapid quenching, allowed for the retention of a high Pt content with thin carbon layers.

High-angle annular dark-field (HAADF) and bright-field scanning transmission electron microscopy (STEM) images (Figure 2B and Supporting Information S1: Figures S3 and S4) of Pt-e-Cn particles reveal a ≈ 300 nm long, non-spherical Pt NP-concentrated carbon matrix nanoscale network with numerous mesopores (Supporting Information S1: Table S2),

26373968, 0, Downloaded from https://onlinelibrary.wiley.com/doi/10.1002/cey2.70300 by Dtsch Zentrum F. Luft-U. Raum Fahrt in D. Helmholtz Gemein., Wiley Online Library on [26/06/2026]. See the Terms and Conditions (https://onlinelibrary.wiley.com/terms-and-conditions) on Wiley Online Library for rules of use; OA articles are governed by the applicable Creative Commons License

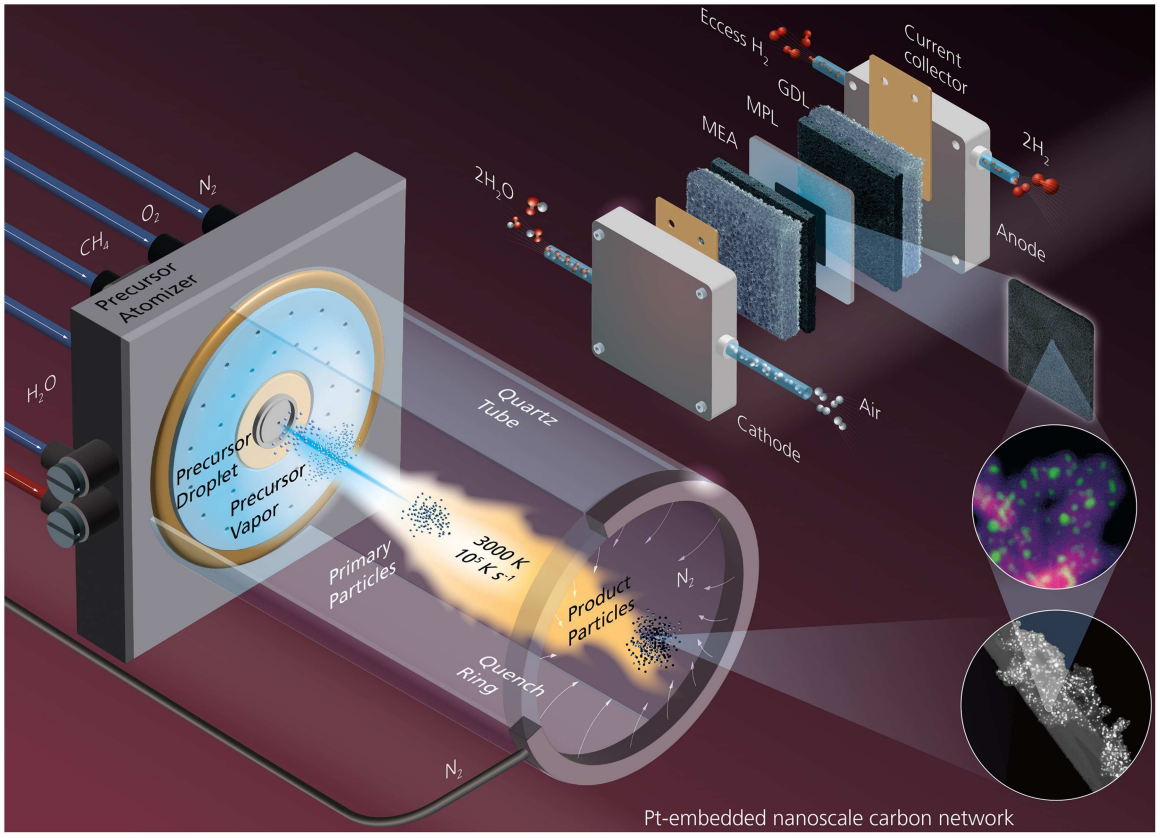

FIGURE 1 | Schematic illustration of our simplified flame spray pyrolysis design, and catalyst structure and their integration in PEM fuel cell architecture.

indicating high accessibility to the Pt vicinity by reactants in the fuel cell operation. The absolute volumes of mesopores and macropores in Pt-e-Cn are approximately fourfold and twofold, respectively, higher than in Pt on mesoporous C_{HSA} (Pt/C_{HSA}), while exhibiting a Brunauer-Emmett-Teller (BET) surface area of 194 $m^2 g^{-1}$ (Figure 2D and Supporting Information S1: Figure S5). These structural characteristics and hierarchical porosity may be advantages for fuel cells requiring enhanced mass transport at high current density [28]. The accessibility to Pt is further facilitated by the thin carbon network, with an average thickness of about 15 ± 8 nm (Figure 2E and Supporting Information S1: Figure S6A,B). Correspondingly, a nearly flat characteristic amorphous carbon signal ($2\theta \approx 20°$) was observed in X-ray diffraction (XRD) patterns (Supporting Information S1: Figure S7) for Pt-e-Cn, compared to Pt/C_{HSA}, suggesting a high disruption of the local carbon structure. This may be caused by the thin carbon matrix with embedded Pt NPs (Figure 2F) of high dispersion (30 ± 2) wt.%. The 2D projection of a 3D structure (Figure 2B), confining all Pt NPs (≈ 650 counts) within the carbon surface, confirms the effective encapsulation of the majority of Pt NPs and the sequential evolution of Pt and carbon, although an accurate measurement of the encapsulating carbon thickness or the nearest distance to access Pt from the carbon surface remains challenging, as shown in Supporting Information S1: Figure S6C,D. This is further supported when investigating the electronic structure via X-ray photoelectron spectroscopy (XPS) (Figure 2G and Supporting Information S1: Figure S8). The Pt $4f_{7/2}$ peak in the high temperature flame-produced Pt-e-Cn (Figure 2G and S8A) appears sharp and in a more reduced state (≈ 71.1 eV), consistent with Pt^0 (71.1–71.5 eV) [29], and remains stable up to 90°C, likely due to the protective carbon layers. In contrast, the Pt $4f_{7/2}$ in Pt/C_{HSA} (Supporting Information S1: Figure S8B) shows a shoulder at higher binding energy (≈ 72.7 eV), resembling the thermally formed PtO_x species (72.8 eV) [30], though distinct from PtO (73.9–74.4 eV) [29]. This additional signal becomes more pronounced after thermal treatment at 90°C. A corresponding decrease in the O 1s signal at elevated temperatures (Supporting Information S1: Figure S8C,D), attributed to desorption of physisorbed oxygen and/or PtO, further supports this interpretation.

The local structure of Pt in Pt-e-Cn was investigated using X-ray absorption spectroscopy and compared with that of Pt/C_{HSA} (Figure 2H–I). The more intense white line in the X-ray absorption near-edge structure spectra (XANES) indicates a higher average Pt oxidation state in Pt/C_{HSA}, whereas Pt in Pt-e-Cn remains only slightly oxidized relative to a Pt foil reference (Figure 2H). This is further supported by extended X-ray absorption fine-structure (EXAFS) analysis (Figure 2I), which reveals a higher intensity of Pt—Pt scattering (Supporting Information S1: Figure S9) relative to the shorter and indistinguishable Pt—O and Pt—C paths [31]. Both Pt-e-Cn and Pt/C_{HSA} exhibit comparable Pt-Pt distances of 2.72–2.74 Å (Supporting Information S1: Table S3); however, Pt-e-Cn shows a larger Pt-Pt coordination number (7.8 vs. 4.0), consistent with a more metallic Pt(0) environment and corresponding to an average particle size of ≈ 1.5 nm [31], in close agreement with TEM measurements (Figure 2F). Three Pt—O(C) paths are resolved for Pt-e-Cn at 1.87, 2.11, and 2.43 Å. The 2.11 Å path lies

26379368, 0, Downloaded from https://onlinelibrary.wiley.com/doi/10.1002/cey2.70300 by Dtsch Zentrum F. Luft-U. Raum Fahrt in D. Helmholtz Gemein., Wiley Online Library on [26/06/2026]. See the Terms and Conditions (https://onlinelibrary.wiley.com/terms-and-conditions) on Wiley Online Library for rules of use; OA articles are governed by the applicable Creative Commons License

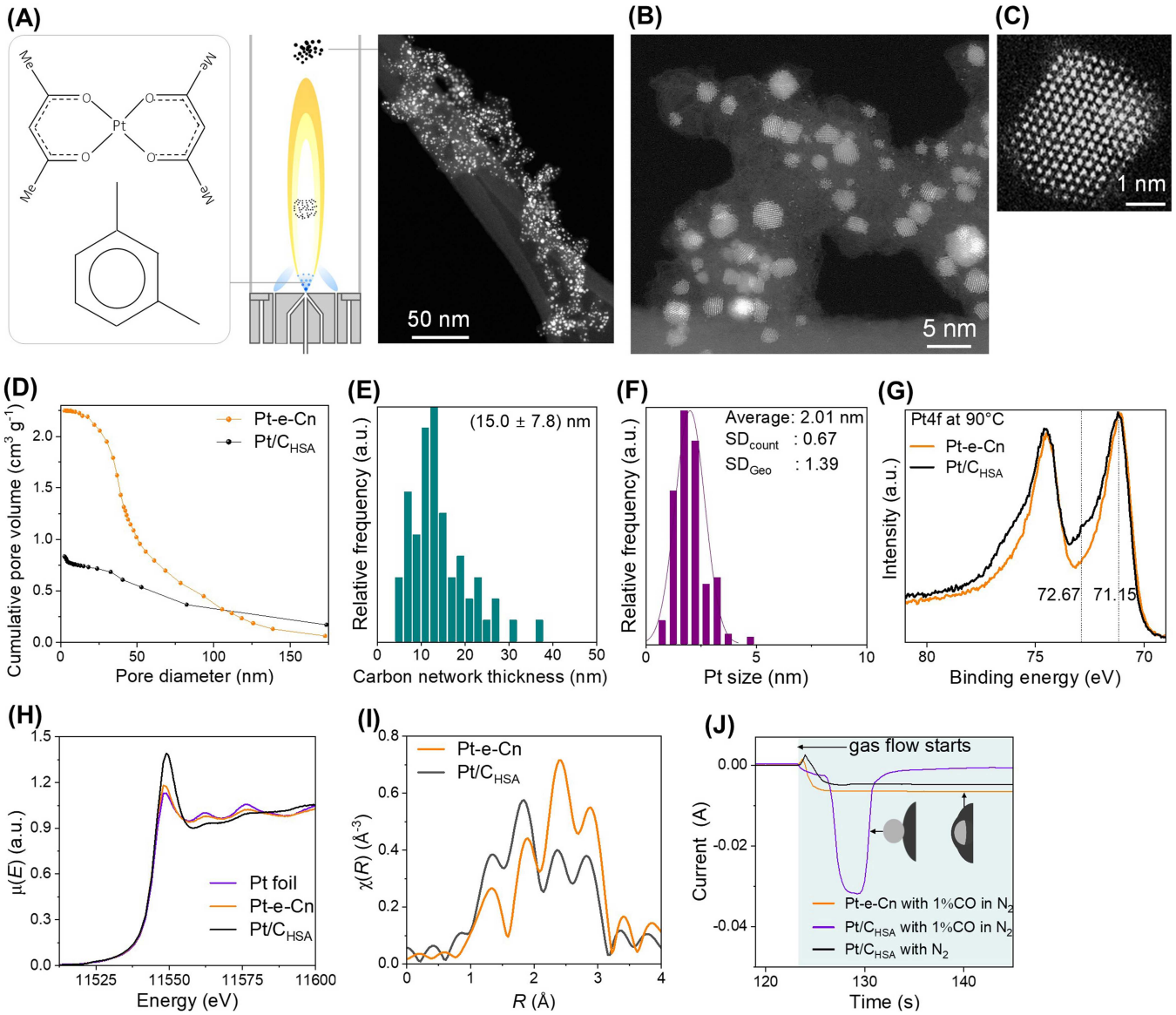

FIGURE 2 | Pt-e-Cn electrocatalyst production and physical characterizations. (A) Schematic illustration of the simplified working principle of atmosphere-controlled FSP-based Pt-e-Cn electrocatalyst production. The atomized precursor solution (left) undergoes numerous stages of transformation through the flame (center), resulting in the Pt-embedded nanoscale carbon network (right) in a one-step process. (B and C) HAADF-STEM images of Pt-e-Cn (B) and a Pt particle within the Pt-e-Cn (C). (D) Cumulative (absolute) pore volume plot for Pt-e-Cn and Pt/CHSA. (E) Carbon network thickness measured from several HAADF-STEM images. (F) Pt 4f intensity normalized XPS of Pt-e-Cn and Pt/C_{HSA} recorded at 90°C. (G) Histogram of the Pt size distribution, estimated from several STEM images of the Pt-e-Cn. The average particle diameter, count, and geometric standard deviations are provided. (H) XANES spectra of Pt-e-Cn collected at the Pt L_3-edge and compared with Pt foil and Pt/C_{HSA} references. (I) Pt L_3 K^3-weighted Fourier-transformed EXAFS spectra of Pt-e-Cn and Pt/C_{HSA}. (J) Current-time response as 1% CO in N_2 (0.25 L min^{-1}) was introduced to pristine fuel cell cathodes with Pt-e-Cn and Pt/C_{HSA} while maintaining a potential hold of 0.55 V. Additionally, current-time response for Pt/C_{HSA} under 100% N_2 flow served as a reference. Measurements were performed at (23 ± 1)°C, 100% relative humidity (RH), and at atmospheric pressure in a differential fuel cell setup without compression. The anode was supplied with 0.25 L min^{-1} of 5% H_2 in N_2.

within error of the Pt—O bond in PtO_2 [32] and can likely be assigned to a $PtO_x(C_x)$ phase. The 2.43 Å Pt-C(O) path also matches the reported Pt—O bonding in cubic PtO [33] or PtC [34] structures. The 1.87 Å path, shorter than the typical Pt—O(C) bonds, aligns with the Pt-C/N bond (1.92 Å) in Pt-embedded graphite layers [35] and molecular Pt carbides (1.899 Å) [36]. Previous studies [37, 38] predict that sub-stoichiometric PtC_x phases or C/H co-adsorption on Pt surfaces can yield Pt—C bond lengths even below 1.80 Å, suggesting that a small fraction of C (≈ 10% based on coordination number) is likely doped into the Pt lattice during Pt-e-Cn formation. Although quantifying these individual phases with overlapping scattering paths in EXAFS is challenging, both Pt-e-Cn and Pt/C_{HSA} can be described as mixtures of Pt, PtO_x, and PtC_x phases.

In addition to isolated Pt atoms and primary Pt clusters (< 1 nm) (Supporting Information S1: Figure S3C,E), the presence of NPs with a mean diameter of (2.01 ± 0.67) nm and a geometric standard deviation of 1.39 (Figure 2F) suggests that the Pt aerosol evolved through coagulation in the free-

26373968, 0, Downloaded from https://onlinelibrary.wiley.com/doi/10.1002/cey2.70300 by Dtsch Zentrum F. Luft-U. Raum Fahrt in D. Helmholtz Gemein., Wiley Online Library on [26/06/2026]. See the Terms and Conditions (https://onlinelibrary.wiley.com/terms-and-conditions) on Wiley Online Library for rules of use; OA articles are governed by the applicable Creative Commons License

molecular regime (1.46 for spherical particles [39]), in the gas phase. Remarkably, the average primary particle size ((2.01 ± 0.67) nm) of Pt-e-Cn is similar to the average crystallite size of (2.7 ± 0.3) nm, as estimated from XRD (Supporting Information S1: Figure S7B), suggesting that most of the primary particles are single crystallites. Contrary to the common belief that high Pt content [24, 39] and temperature cause metal particle coarsening, Pt NPs show a narrow size distribution when produced by FSP. The short high-temperature exposure, in the range of milliseconds, of gas-phase Pt, followed by rapid cooling (up to 10^5–10^6 K s^{-1}) [18] and carbon growth on Pt, helps preserve the homogeneous structure and morphology of Pt-e-Cn, which is strictly controlled by the process parameters, including precursor and O_2 feed rates, and quench flow and distance. It shows further promises for extending this method for embedding alloys [40] and thermal shock-stabilized solid solutions [18].

While 2D STEM imaging provides insights into the local catalyst structure, it does not quantitatively resolve the extent of carbon coverage on the Pt surface. To assess this, carbon monoxide (CO) displacement measurements [12] were performed in a fuel cell setup utilizing as-synthesized (pristine) Pt-e-Cn and compared with commercial Pt/C_{HSA} under identical conditions (Figure 2J and Supporting Information S1: Figure S10). In Pt/C_{HSA}, introducing 1% CO in N_2 induces a reductive current, attributed to zero-charge CO physically displacing pre-adsorbed species from the Pt surface. Conversely, for Pt-e-Cn, the current remains identical to the reference baseline recorded under 100% N_2 flow for Pt/C_{HSA}, explaining the absence of CO displacement charge. This confirms that the Pt surface is predominantly covered by carbon layers, effectively limiting CO adsorption.

2.2 | Pt-e-Cn Performance and Structural Evolution in Fuel Cells

To evaluate the ORR performance of Pt-e-Cn under fuel cell-relevant conditions, single cell measurements were conducted using a 12 cm^2 active area and benchmarked against commercial Pt/C_{HSA} under identical conditions. Half-cell measurements were also performed to assess intrinsic catalytic activity (Supporting Information S1: Figure S11 and related content) and to screen catalysts produced during fundamental particle optimization via FSP conditions. Despite being embedded in a thin carbon matrix, Pt-e-Cn demonstrated 10% higher ORR mass activity than Pt/C_{HSA}, suggesting effective reactant access to Pt active sites and uncompromised oxygen reduction activity. For single-cell evaluation, membrane electrode assemblies (MEAs) were prepared by spraying the catalyst ink onto the membrane. Details of catalyst ink formulation, coating, MEA preparation, and cell test conditions are provided in the Methods.

The cell was conditioned to activate the catalyst prior to the beginning-of-test (BOT), followed by an accelerated stress test (AST) protocol (Supporting Information S1: Table S4), including intermediate and end-of-test (EOT) characterizations, to induce and evaluate catalyst degradation. Notably, Pt-e-Cn required 1200 load cycles in H_2-Air and 10 cyclic voltammetry (CV) sweeps to achieve 98% of maximum performance (2.65 A cm^{-2} at 0.4 V) (Supporting Information S1: Figure S12). This contrasts with the Pt/C_{HSA} catalyst, which required only 100 load cycles, implying an initial high resistance to oxygen permeation through the carbon overlayer for Pt-e-Cn. Thus, activation is an important aspect of the utilization of catalysts with protective overlayers. An increase in performance was observed for both the catalysts over 1k cycles, signaling overlap between activation and degradation processes. While the cell with Pt/C_{HSA} exhibited higher initial performance (1.20 W cm^{-2} at peak) compared to Pt-e-Cn (1.06 W cm^{-2}) (Figure 3A), the Pt/C_{HSA} performance started to decrease drastically after 1k AST cycles, retaining only 80% of BOT performance at 0.5 V after 10k cycles (Figure 3B). Similar behavior was reported by Stariha et al. [41] for PEMFC with cathode Pt loading of 0.15–0.2 mg cm^{-2}, showing ≈60% electrochemical active surface area (ECSA) loss after 10k AST cycles. In contrast to these observations, Pt-e-Cn nearly retained (Figure 3C) its performance and surpasses Pt/C_{HSA} performance across the entire potential range from the kinetics-dominated to the transport-dominated regime of the polarization curves (Figure 3D and Supporting Information S1: Figure S13). While Pt/C_{HSA} continues to lose performance after 10 k cycles (Figure 3D), exhibiting a 35% decrease at 0.5 V and 53% at 0.8 V after 30k cycles, Pt-e-Cn demonstrates exceptional durability with only a negligible 3% loss of BOT performance at 0.5 V and a slight gain at 0.8 V, suggesting potential access to additional Pt surface.

With its high-performance retention, Pt-e-Cn meets the DOE targets for cell voltage losses at 0.8 and 1.5 A cm^{-2} and qualitatively surpasses the durability of recently reported electrocatalysts (Figure 3E and Supporting Information S1: Table S5) [42–58], with minimal power loss (Supporting Information S1: Figure S13E) comparable to reported catalysts. Although a direct quantitative comparison with literature is not possible due to differences in single-cell test conditions, including catalyst loading, membrane thickness, flow field, H_2-air flow rate, back pressure, humidity, and temperature (Supporting Information S1: Table S5). In contrast, a reliable durability comparison between Pt-e-Cn with lower initial power and Pt/C_{HSA} is feasible within the 10k and 30k AST window, where rated power loss stabilizes (20%–22% for Pt/C_{HSA}) with negligible influence of activation-related cell voltage evolution, and power densities converge (Supporting Information S1: Figure S13F). Within this window, Pt-e-Cn exhibits less than 5% degradation rate, corresponding to at least a fourfold lower degradation than Pt/C_{HSA}. This highlights the true durability of flame-made Pt-e-Cn structure without an activity trade-off, making it suitable for long-life heavy-duty applications. Although the achieved performance does not meet the EU CH-JU 2030 target, both Pt-e-Cn and Pt/C_{HSA} exhibit similar performance after extended AST under identical MEA configurations. This indicates that the performance gap is influenced by the MEA architecture and its evolution during testing, and highlights the potential for further improvement through optimization of membrane thickness and advanced electrode fabrication strategies.

Similarly, the ECSA loss calculated from the hydrogen underpotential deposition (H_{upd}) region and CO stripping charges for Pt-e-Cn (12% and 4%, respectively) is significantly lower than

26373968, 0, Downloaded from https://onlinelibrary.wiley.com/doi/10.1002/cey2.70300 by Dtsch Zentrum F. Luft-U. Raum Fahrt in D. Helmholtz Gemein., Wiley Online Library on [26/06/2026]. See the Terms and Conditions (https://onlinelibrary.wiley.com/terms-and-conditions) on Wiley Online Library for rules of use; OA articles are governed by the applicable Creative Commons License

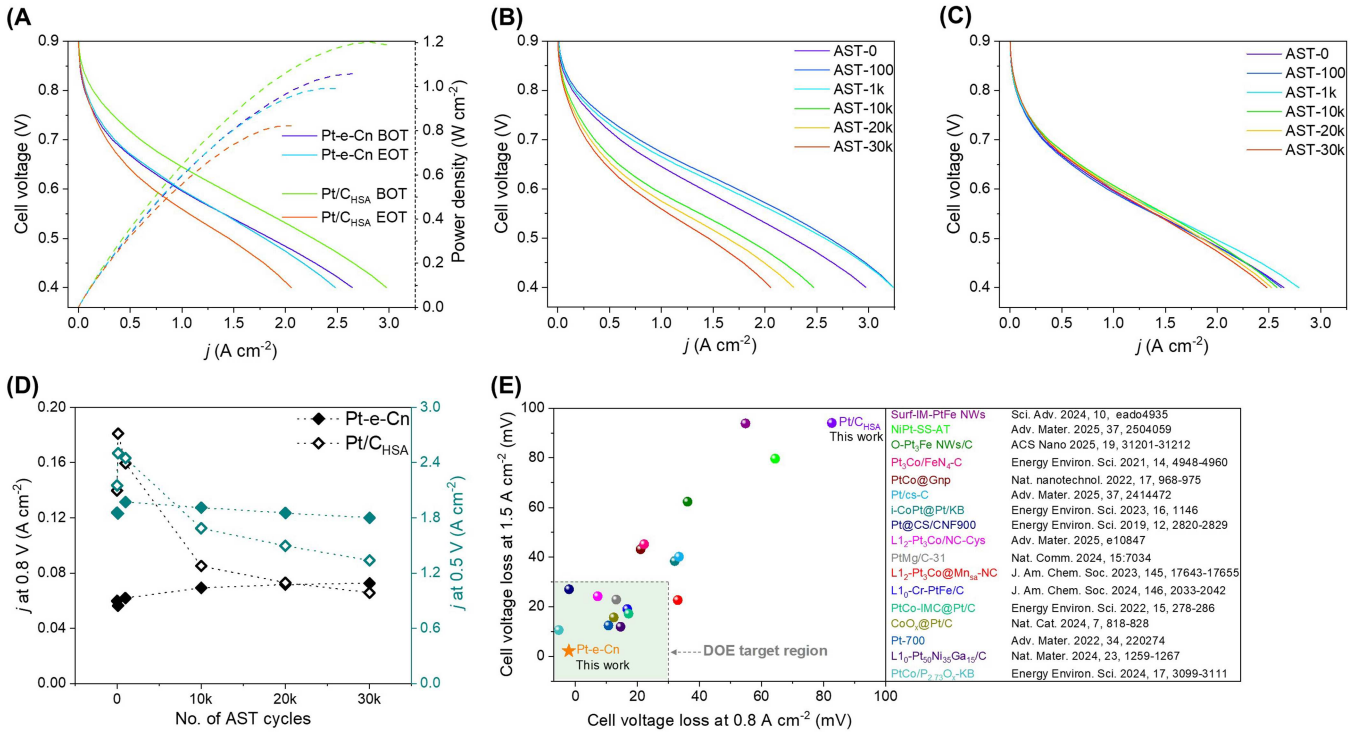

FIGURE 3 | MEA performance of Pt-e-Cn as PEMFC cathode electrocatalyst in comparison with Pt/C_{HSA}. (A) H_2-air fuel cell polarization (left axis) and power density (right axis) plots of Pt-e-Cn and Pt/C_{HSA} at the BOT (activated) and EOT (after 30k AST cycles). (B and C) H_2-air fuel cell polarization plots of Pt/C_{HSA} (B) and Pt-e-Cn (C) obtained at six stages of the AST test, highlighting the superior durability of the MEA with Pt-e-Cn. (D) Current density as a function of AST cycles for Pt-e-Cn (solid symbols) and Pt/C_{HSA} (hollow symbols) at 0.8 V (kinetic region; left-axis) and 0.5 V (ohmic/transport region; right-axis). (E) Comparison of cell voltage losses at 0.8 and 1.5 A cm^{-2} in H_2-air conditions after AST for Pt-e-Cn (this work), a reference catalyst (Pt/C_{HSA}), and SoA electrocatalysts reported in recent literature. DOE targets (30 mV) for both cell voltage losses are marked by dashed lines and highlighted in green. Due to differences in single-cell test conditions of these catalysts, this chart is intended only for a rough comparison of voltage losses; details on test conditions are provided in Supporting Information S1: Table S5.

the corresponding losses observed for Pt/C_{HSA} (65% and 57%, respectively; Figure 4A). Notably, the change in ECSA by CO stripping (4%), which is less affected by hydrogen crossover and capacitive currents compared to ECSA by H_{upd}, closely matches the changes in cell voltage losses (up to 3%), indicating that variations in cell power output are linked to metal dissolution. The modest loss of ECSA indicates that the emergence of a fresh accessible Pt surface is minimal. Therefore, the lower ECSA loss may result from changes in the Pt surface, protective layer, and double layer capacitance (C_{dl}), as discussed below. With its exceptional ECSA retention at EOT, Pt-e-Cn satisfies the stringent DOE degradation target, outperforming values reported in recent literature (Figure 4B and Supporting Information S1: Table S5) [42–48].

The Pt-e-Cn initially exhibits Pt(110) characteristics largely in the H_{upd} region, which gradually evolves due to potential-induced transformations [59] into thermodynamically equilibrated Pt polycrystalline NPs with similar ORR activity. Unlike the typical and continuous depletion of Pt(110), Pt(100), and Pt(111) surfaces in polycrystalline Pt/C_{HSA} throughout the durability tests (Supporting Information S1: Figure S14A,B), Pt-e-Cn shows relatively increasing fractions of dense Pt(100) and Pt(111) facets, which have higher intrinsic capacitance (Figure 4C and Supporting Information S1: Table S6). This evolution could drive minimal Pt dissolution [60] and sintering under ORR conditions, but also seems to be accountable for the observed fivefold lower ECSA loss. While the performance of Pt-e-Cn in H_2-Air is roughly comparable to that of Pt/C_{HSA} after 5-10k AST (Figure 3B), its ORR signal in H_2-N_2 is relatively negligible (Supporting Information S1: Figure S14C,D). This is in correlation with minimal formation and oxidation of adsorbed hydroxyl groups (OH_{ads}) on the hydrophilic Pt surfaces, which depend on specific water adlayers [61]. This observation holds true across varying scanning potential ranges up to 1.0 V, suggesting that the shift in the OH_{ads} onset is not due to SO_4^- adsorption on the Pt surface. Instead, it points to a more packed structure of Pt surfaces, effectively increasing oxidation potential [62]. This supports that the stable Pt surface is largely protected against surface oxidation by interaction with a porous carbon overlayer (will be discussed later). As a result, the Pt-e-Cn electrocatalyst fulfills the EU Clean Hydrogen Joint Undertaking's 2030 target of less than 10% performance loss, even with lower Pt loading. While the ECSA of Pt-e-Cn remains nearly constant, the 155% increase in C_{dl} (Supporting Information S1: Figure S14E) compared to a 20% decrease for Pt/C_{HSA} suggests an enhanced electrochemically accessible interface within the catalyst layer (CL), likely associated with improved wettability by surface oxidation of carbon and formation or enlargement of porous channels within the nanoscale network. This evolution may enhance reactant transport to active sites, potentially offsetting performance or ECSA loss during the operation.

26379368, 0, Downloaded from https://onlinelibrary.wiley.com/doi/10.1002/cey2.70300 by Dtsch Zentrum F. Luft-U. Raum Fahrt in D. Helmholtz Gemein., Wiley Online Library on [26/06/2026]. See the Terms and Conditions (https://onlinelibrary.wiley.com/terms-and-conditions) on Wiley Online Library for rules of use; OA articles are governed by the applicable Creative Commons License

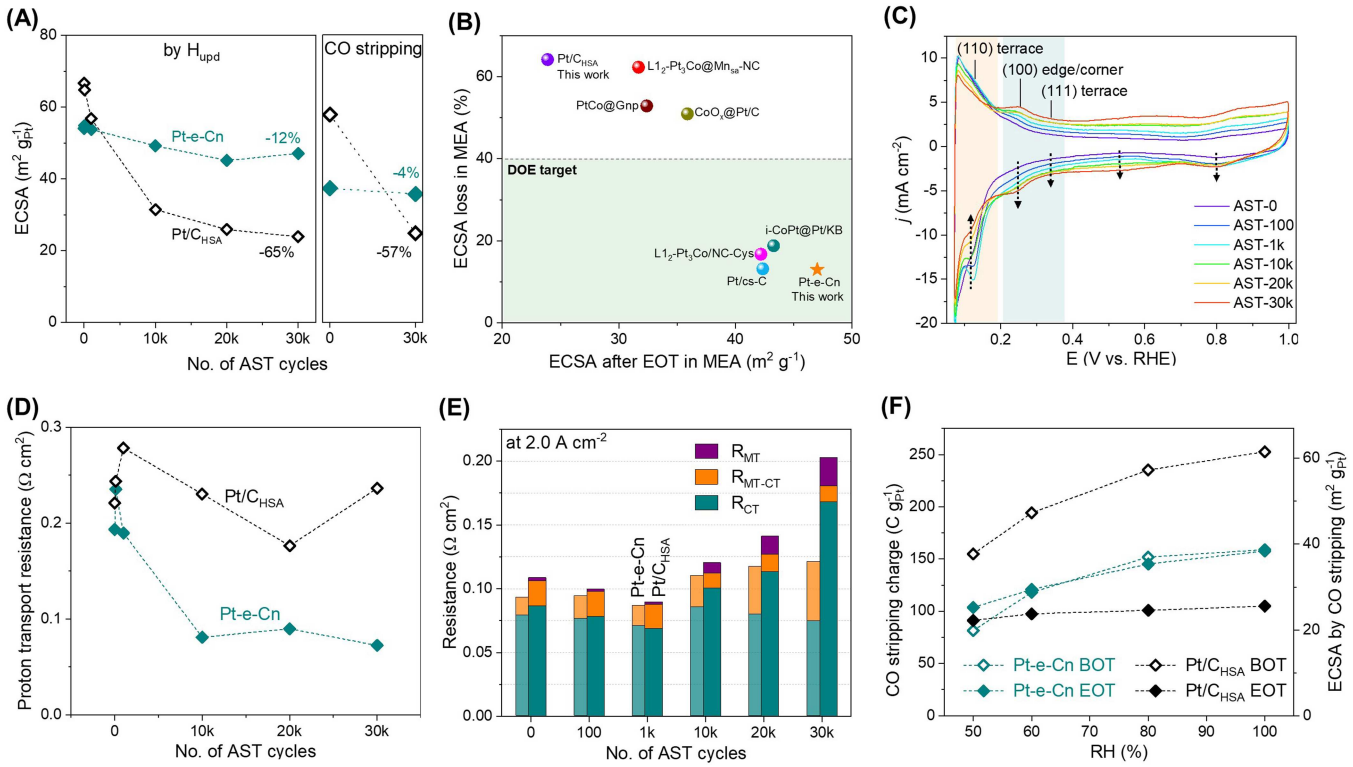

FIGURE 4 | Further electrochemical characterization of Pt-e-Cn as PEMFC cathode electrocatalyst in comparison with Pt/C_{HSA}. (A) ECSA as a function of AST cycles for Pt-e-Cn and Pt/C_{HSA}, calculated from H_{upd} adsorption region of the corresponding CV at 80°C and 80% RH (Supporting Information S1: Figure S14) and from the CO stripping CV measurements at 40°C and 80% RH (Supporting Information S1: Figure S18). (B) comparison of percentage ECSA loss with specific ECSA at EOT after AST for Pt-e-Cn (this work), a reference catalyst (Pt/CHSA), and SoA electrocatalysts reported in recent literature. DOE target for ECSA loss in single cells is marked by dashed lines and highlighted in green. (C) Evolution of cyclic voltammetry characteristics as a function of AST cycles for Pt-e-Cn, marked with Pt(110) region (0.08 to 0.2 V) in yellow and Pt(100) region (0.2 to 0.36 V) in green, and the relatively less pronounced Pt(111) peak. (D) Effective proton transport resistance. (E) Charge transfer and transport resistances at 2 A cm^{-2} for Pt-e-Cn and Pt/C_{HSA}. R_{CT}, $R_{CT\text{-}MT}$, and R_{MT} refer to charge transfer resistance, charge transfer reaction-influenced mass transport resistance, and mass transport resistance, respectively. It is noted that for Pt-e-Cn, R_{MT} was set to zero for all cases due to the absence of a low-frequency semicircle. (F) Effects of relative humidity at a cell temperature of 40°C on the CO stripping charges (left-axis) and corresponding ECSA (right-axis) for Pt-e-Cn (green symbols) and Pt/C_{HSA} (black symbols) at BOT (after activation) and EOT (after 30k AST cycles).

Despite its higher intrinsic activity in half-cell tests, Pt-e-Cn exhibits lower performance in the MEA kinetic region, particularly during the initial stages (up to 1000 AST cycles). This discrepancy is attributed to differences in the initial interfacial state of the CL. In particular, the embedded structure and reduced ionomer-Pt interaction in Pt-e-Cn may limit local proton accessibility under low-current conditions at early stages. During operation, however, the Pt-e-Cn exhibits continuous and favorable structural evolutions, including in C_{dl} and Pt facets over extended AST cycles (Figure 4C), while maintaining stable ECSA and performance. In contrast, Pt/C_{HSA} shows minimal evolution during the initial stages but undergoes rapid loss of ECSA and performance upon continued AST. These results suggest that, while half-cell probes measure the intrinsic activity of the catalysts under idealized conditions, MEA performance is influenced by the interfacial structure and its evolution. In this context, Pt-e-Cn benefits from progressive improvement in accessibility to carbon and Pt surfaces, as well as enhanced wetting and ionomer distribution (discussed later).

The effective proton transport resistance (R_{H+}) in the Pt-e-Cn cathode electrode is measured by electrochemical impedance spectroscopy (EIS; Figure 4D and Supporting Information S1: Figure S15) in H_2-N_2. R_{H+} sharply decreased by ≈ 50% from 100 to 10k AST cycles and then remained nearly stable, mirroring the trend observed in C_{dl}. Considering that the proton transport is directly linked to water content in the CL, it again suggests an increase in water uptake of the CL and thus the membrane (Supporting Information S1: Figure S16), likely due to enhanced hydrophilicity of the carbon surface by OH groups and redistribution of ionomer. Whereas a nearly twofold higher but steady R_{H+} during AST was observed for Pt/C_{HSA} (Supporting Information S1: Figure S15). The steeply sloped lines above the 45° regions in Pt/C_{HSA} mark relatively high surface accumulation of water that would be located in the ionomer [63].

EIS was used to monitor impedance evolution under H_2-air operating conditions at current densities between 0.2 and 2 A cm^{-2} (Supporting Information S1: Figures S15 and S17). Regardless of current densities, resistance to ORR charge transfer (R_{CT}) did not show significant changes over 30k cycles (< 12% increase) in the Pt-e-Cn electrode, while Pt/C_{HSA} exhibited a dramatic 94% increase during the aging test (Figure 4E). This aligns with the evolution of polarization curves at low current densities, where charge transfer processes

26373968, 0, Downloaded from https://onlinelibrary.wiley.com/doi/10.1002/cey2.70300 by Dtsch Zentrum F. Luft-U. Raum Fahrt in D. Helmholtz Gemein., Wiley Online Library on [26/06/2026]. See the Terms and Conditions (https://onlinelibrary.wiley.com/terms-and-conditions) on Wiley Online Library for rules of use; OA articles are governed by the applicable Creative Commons License

dominate. This confirms that the electrode with the nanoscale network ensures robust electron and proton transport as well as catalyst activity, thanks to the stability of the active area and the evolution of a more accessible pore structure. While equivalent circuit-based analysis is model-dependent, it provides useful insights into changes in low-frequency response associated with mass transport processes. Supporting Information S1: Figure S17A shows that the radius of the R_{CT} semicircle is also affected by an additional semicircle at lower frequencies, which can be described by the mass transfer processes representing a charge transfer reaction-influenced mass transport resistance ($R_{MT\text{-}CT}$) [64], for both Pt-e-Cn and Pt/C_{HSA} electrodes at 2 A cm^{-2}. While $R_{MT\text{-}CT}$ continues to increase slowly in Pt-e-Cn over cycling, an additional diffusive feature at low frequencies eventually emerged in Pt/C_{HSA}, indicating increasingly complex transport limitations likely associated with O_2 mass transport (R_{MT}) (Supporting Information S1: Figure S17A). There is no consensus on the R_{MT} interpretation; it is likely due to liquid water accumulation [64] in the CL or the interface between CL and the gas diffusion layer. R_{MT} and R_{CT} increase strongly in Pt/C_{HSA} CL from 10k AST cycles, revealing acceleration of catalyst degradation upon cycling. Overall, a 69% lower transfer/transport resistance observed for CL with Pt-e-Cn than Pt/C_{HSA} supports that the stable performance is a result of its enhanced reactant transport properties and stable catalytic activity.

2.3 | The Origin of the High Durability

To assess the degree of protection, CO stripping measurements (Figure 4F and Supporting Information S1: Figure S18) were conducted at 40°C across varying relative humidity (RH) levels, following Garrick et al. and Shinozaki et al. and their conclusions [12, 65]. This was done considering that the electrochemical oxidation of CO at the Pt surface requires access to water and protons, either through ionomer or condensed water in the CL, and that Pt located within pores exhibits reduced proton accessibility at low RH [12, 65]. At BOT, the activated Pt-e-Cn shows a relatively lower CO stripping charge across the selected RH range, with a trend similar to Pt/C_{HSA} (Figure 4F and Supporting Information S1: S18A,B). Notably, at 80% RH, the ECSA derived from the CO stripping charge of Pt-e-Cn is 35% less than that of Pt/C_{HSA}. It implies the fraction of protected interior Pt (in carbon pores) in Pt-e-Cn is less compared to in high surface area Pt/C_{HSA}, marking relatively less protection from ionomer poisoning at BOT. However, the trend changes drastically after operation (EOT) for Pt/C_{HSA}. It shows a nearly flat response to RH change, similar to low surface area Vulcan carbon-supported Pt without mesoporosity [12, 65], and about 57% reduction in CO stripping charge at 80% RH. Corresponding changes in CO stripping-based ECSA (Figure 4F) are well comparable to a 65% decrease in ECSA estimated from H^+_{ads} (Figure 4A) at 80% RH and 80°C. Since CO adsorption occurs on ionomer-free Pt surfaces, the 57% reduction in CO stripping-based ECSA suggests that Pt/C_{HSA} is more vulnerable to Pt degradation processes upon operation. In contrast, Pt-e-Cn shows excellent retention of CO stripping charge across varying RH (Supporting Information S1: Figure S18C), with only 4.3% decrease at 80% RH after EOT, underscoring the exceptional durability of the embedded Pt structure. The CO stripping charge at 50% RH after EOT slightly exceeds that at BOT, suggesting possible pore enlargement, consistent with the observed increase in C_{dl}. Moreover, a large fraction of ionomer-free active Pt surface ($\approx$ 40% of 39 $m^2\,g_{Pt}^{-1}$; see Supporting Information S1: Table S7 for more details on different properties) still remains within mesoporous channels accessible at > 50% RH. This qualitatively indicates lower susceptibility of Pt-e-Cn to ionomer poisoning during operation. This is further supported by the evolution of displacement charge coverage (θ_{dis}; Figure S18E,F) at varying relative RH, following the method used by Garrick et al. [12, 66] For Pt-e-Cn, the apparent coverage either decreases or remains stable at varying RH upon testing, accompanied by negligible ECSA loss, indicating suppressed further accumulation of surface-blocking species and preserved catalyst accessibility. For Pt/C_{HSA}, the increased coverage alongside a substantial 57% ECSA loss suggests enhanced adsorption of surface-poisoning species.

While partial separation of Pt nanoparticles embedded within the carbon network from direct ionomer adsorption reduces surface poisoning, it may also limit local proton accessibility to some extent. However, the observed MEA performance and RH-dependent behavior indicate that proton accessibility is maintained under operating conditions. Notably, effective proton transport does not require direct ionomer coverage of all Pt surfaces [67, 68], but rather depends on the local catalyst-ionomer interface. In this context, proton transport in the CL may occur through short-range conduction from adjacent ionomer domains, and water-mediated pathways [67, 68], in addition to thin ionomer films.

Atomic force microscopy (AFM) measurements were performed to assess the surface morphology and electronic conductivity of the pristine, activated, and AST-tested CL with Pt-e-Cn (Figure 5A–D and Supporting Information S1: Figures S20–S25). Surface and cross-sections were measured to assess the top surface properties as well as the internal structure of the catalyst coated membrane (CCM). In contrast to the Pt/C_{HSA} CL surface, where the electronically conductive area increases from $\approx$30% to over $\approx$68% at a bias of 1 V after the degradation test (Supporting Information S1: Figure S20), the Pt-e-Cn experiences a homogeneous and drastic decrease in the conductive surface area. For Pt-e-Cn, it drops from over 95% in the pristine CL to $\approx$38% after activation and to below 20% after AST-testing (Figure 5A–C). However, this trend gradually reverses across the CL cross-section, showing a reduction of conductivity of Pt-e-Cn CL toward the CL/PEM interface extending up to 3 μm (Figure 5D and Supporting Information S1: Figure S22). The reduction in conductive surface area at the surface can be attributed to ionomer redistribution, increasing contact resistance—likely due to PTFE transfer from microporous layer—and/or changes in CL pore volume. The reduction close to the interface may result from platinum dissolution or ionomer redistribution, suggesting that degradation primarily occurs at the membrane-CL interface, with minimal effects away from the interface. For Pt/C_{HSA}, the change in conductive area was severe on the top surface as well as the cross-section (Supporting Information S1: Figures S20 and S23). This is further supported by high-resolution scanning electron microscopy (HR-SEM) images on the CL cross-section (Figure 5E–H and Supporting Information S1: S26), which reveal a slight increase in macro pore (> 50 nm) area (Supporting Information S1: Figure S27) for the post-AST

26373968, 0, Downloaded from https://onlinelibrary.wiley.com/doi/10.1002/cey2.70300 by Dtsch Zentrum F. Luft-U. Raum Fahrt in D. Helmholtz Gemein., Wiley Online Library on [26/06/2026]. See the Terms and Conditions (https://onlinelibrary.wiley.com/terms-and-conditions) on Wiley Online Library for rules of use; OA articles are governed by the applicable Creative Commons License

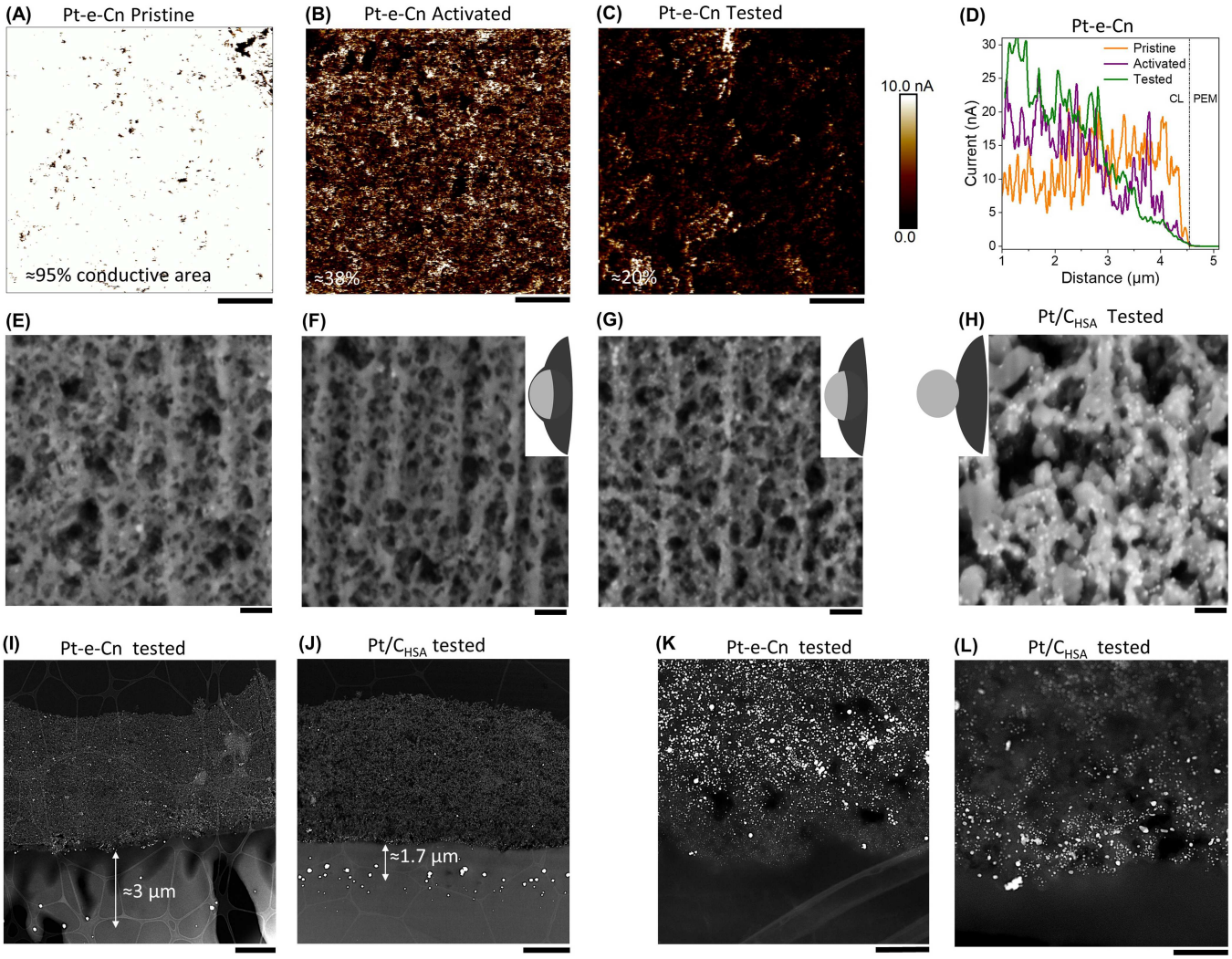

FIGURE 5 | Microscopic characterization of catalyst layers with Pt-e-Cn as the cathode electrocatalyst. (A–C) AFM electronic conductivity mapping on the surface of the pristine (A), activated (B), and AST-tested (C) CCL with Pt-e-Cn, with the corresponding percentage of conductive area indicated in each panel. Scale bars: 600 nm. Intensity bars are on the right side. (D) Line profile of AFM electronic conductivity measurements on the cross-section of the pristine, activated, and AST-tested Pt-e-Cn CCL-PEM interface obtained from Supporting Information S1: Figure S22. The widths of the scanned lines were ≈100 nm. E-H, SEM images on the cross-section prepared by FIB of the pristine (E), activated (F), and AST-tested (G) CCL with Pt-e-Cn, and AST-tested CCL with Pt/C$_{HSA}$ (H). Scale bars: 100 nm. Insets in (E) and (H): scheme representing possible Pt (light gray) and carbon (dark gray) arrangement. HAADF-STEM images of the catalyst layers at different magnification: (I and J) tested CCL with Pt-e-Cn (I) and Pt/C$_{HSA}$ (J). Scale bars 2 μm. Arrow marks indicate the average distance between the membrane and the Pt band. (K and L) Tested Pt-e-Cn (K) and Pt/C$_{HSA}$ (L) CCL-PEM interface. Scale bars 200 nm.

Pt-e-Cn. In contrast, the Pt/C$_{HSA}$ shows a reduction in the macro pore area with a corresponding increase in the conductive area of the CL front (Supporting Information S1: Figures S23–S24). The difference in macro pore area between the CLs with Pt-e-Cn and Pt/C$_{HSA}$ increases from < 1% (for pristine CLs) to up to 6% (for tested CLs). However, this small enlargement in pore volume cannot be directly linked to the observed 155% increase in C_{dl}. Instead, C_{dl} likely reflects changes in interfacial properties such as improved wettability, surface oxidation, and ionomer distribution within the catalyst layer.

Figure 5E–G shows the noticeable emergence of Pt NPs in the aged Pt-e-Cn CL. Yet, compared to Pt in Pt/C$_{HSA}$ (Figure 5H), these Pt NPs remain partially embedded within the carbon matrix, making them less vulnerable to degradation processes. Whereas the operated Pt/C$_{HSA}$ exhibits pronounced non-uniform Pt growth (Figure 5H) relative to its pristine state (Supporting Information S1: Figures S29 and S30), indicative of coalescence- and coarsening-driven degradation of the Pt residing on the carbon surface, unlike Pt NPs in the mesopores [69]. This is further evident in 100-nm-thick MEA cross-sections after the AST (Figure 5I–J and Supporting Information S1: Figure S31). The area-normalized concentration of migrated Pt forming the Pt band, ≈3 μm away from the membrane, as a result of redeposition [44], is ≈2.4-fold lower for Pt-e-Cn than for Pt/C$_{HSA}$ (Supporting Information S1: Figure S32). Moreover, a shorter distance between the cathode catalyst layer (CCL) and Pt band (Figure 5J), along with the presence of agglomerates near the CCL-PEM interface (Figure 5L and Supporting Information S1: Figure S33C) in Pt/C$_{HSA}$, suggests continuing dissolution of Pt. In contrast, uniformly distributed Pt NPs (< 1 nm) at the Pt-e-Cn cathode front near the membrane (Figure 5K and

26373368, 0, Downloaded from https://onlinelibrary.wiley.com/doi/10.1002/cey2.70300 by Dtsch Zentrum F. Luft-U. Raum Fahrt in D. Helmholtz Gemein., Wiley Online Library on [26/06/2026]. See the Terms and Conditions (https://onlinelibrary.wiley.com/terms-and-conditions) on Wiley Online Library for rules of use; OA articles are governed by the applicable Creative Commons License

Supporting Information S1: Figure S33A,B) support significantly low Pt mass loss into the membrane. This high durability of Pt-e-Cn can be attributed to the co-growth of Pt particles and carbon nanoscale network during FSP synthesis, and the carbonization of native ligand from the precursors [55], which enhances Pt-carbon interactions and results in electronic effects and modulates the structural durability of the catalyst for the ORR at low Pt load and I/C ratio. Detailed theoretical studies on these interactions are reserved for future work.

3 | Conclusions and Perspective

We have presented a functional high-surface-area carbon nanonetwork-embedded catalyst structure produced via a highly scalable and cost-efficient FSP technique in a single process step. Upon proper activation, the gas-phase-produced, highly dispersed Pt nanocatalysts (≈ 2 nm) show exceptional durability and uncompromised performance after > 1k AST. It retained 97% of power output at 0.5 V and 88% of ECSA after extensive durability testing in a low-Pt-content PEMFC, significantly outperforming start-of-the-art catalysts. The Pt-e-Cn electrode retains 96% of the ionomer-free active Pt surface, exhibits efficient H^+ conductivity and O_2 mass transport characteristics, mitigates accumulation of Pt surface-blocking species, coalescence, and coarsening upon operation, and lowers Pt dissolution by 2.4-fold, alongside maintaining uniform redistribution of electronic conductivity. The enhanced durability of the PEMFC can be attributed to the remarkably continuous and favorable evolution of both the catalyst and catalyst layers, as well as the strong coordination between protected Pt nanoparticles and their surface-grown co-synthesized carbon matrix. Overall, the results indicate that both intrinsic catalyst stability and catalyst layer restructuring contribute to the performance evolution of Pt-e-Cn. A comprehensive understanding of these effects will require additional analyses, including limiting current analysis, extended durability testing under dynamic load cycling, and porosimetry on CL, which will be addressed in future work.

Beyond Pt-e-Cn, this advancement can be extended to other material classes produced by FSP, including alloy catalysts (such as PtNi-e-Cn; Supporting Information S1: Figure S34) with high intrinsic activity but limited stability, and heteroatom-doped carbon nanonetworks (e.g., nitrogen- and sulfur-doped) to further enhance performance. Overall, this work demonstrates an alternative approach for designing more durable metal-C-based nanonetwork electrocatalysts directly from metal-nuclei through an unconventional, scalable, and economically viable production technique for highly demanding reactions in fuel cells, and extendable to electrolyzers and batteries.

4 | Methods

4.1 | Catalyst Synthesis

Pt-e-Cn with a (30 ± 2) wt.% Pt was synthesized using FSP techniques (Supporting Information S1: Figure S1). A precursor solution containing platinum(II) acetylacetonate (Pt source) dissolved in xylenes (the primary carbon source) at a final Pt concentration of 25 mM was atomized at a flow rate of 4 mL min^{-1}, using 4 L min^{-1} oxygen as dispersion gas at a pressure of 1.8 bar. The spray was ignited by a support flame fueled by 1 L min^{-1} CH_4 and 2 L min^{-1} O_2, generating a high-temperature spray flame. To establish a controlled oxygen-lean atmosphere, (i) a quartz or stainless-steel tubular enclosure (55 mm in diameter and 300 mm in length) was used around the flame, (ii) a shroud gas flow of 40 L min^{-1} N_2 was introduced in between the flame and the enclosure, and (iii) a quench gas flow of 5 L min^{-1} N_2 was introduced just above the enclosure at an angle that facilitated the narrow upward transportation of nanoparticles. In addition to preventing atmospheric air entrainment into the reactor, the use of shroud and quench gases reduced nanoparticle deposition onto the enclosure and halted further catalyst evolution by enhancing the cooling rate of the flame aerosol, respectively. With a 12 min FSP run, approximately 0.5 g of Pt-e-Cn was collected on a sampling glass fiber filter (GFF) disk positioned 60 cm above the atomizer and used without further processing. The overall yield of the FSP synthesis was not quantified, as a significant fraction of the generated powder was lost to the dust collection chamber of the lab-scale FSP setup. In an industrial-scale production, after the implementation of proper production rate optimization, the product powder would be directly collected in a collection chamber for a higher yield. The Pt-e-Cn powder was then treated at 500°C in NH_3 atmosphere for 30 min.

4.2 | Physicochemical Characterization

The phase characteristics of the as-synthesized samples were analyzed using Bruker D8 XRD. To ensure a flat surface and minimize air scattering, the samples were ground prior to analysis. A low background holder with a small powder volume was used, and diffraction patterns were recorded over a 5°–90° 2θ range using a 1D detector. The crystallite size was determined from XRD data using the Debye-Scherrer equation.

The Pt content in Pt-e-Cn was determined by inductively coupled plasma mass spectrometry (ICP-MS) [70] using an XSeries2 device from Thermo Fisher Scientific. Briefly, 2 mg of Pt-e-Cn was digested in a mixture of HCl and HNO_3 for 12 h to dissolve Pt. The solution was then filtered and diluted with 2 wt.% HNO_3. Pt calibration solutions with varying Pt concentrations were prepared using a certified Pt ICP standard (Carl Roth). The signal intensities of the ^{194}Pt, ^{195}Pt, and ^{196}Pt isotopes were used to determine the Pt content, yielding a value of 28.3 wt.%.

The approximate elemental composition (Pt and C wt.%) of the as-synthesized powders was also determined using a Zeiss Crossbeam 350 SEM equipped with an energy dispersive spectroscopy (EDS) system (Oxford Instruments), operated at an acceleration voltage of 2–5 kV and a working distance of 5 mm. The powder sample was gently compressed onto the sample holder to reduce the surface porosity and improve flatness. The reported composition represents the average of over 15 measurements taken at distinct spots. To ensure the reliability of sample preparation and measurement, Pt/C_{HSA} with a known composition was employed as a calibration standard. The cross-sectional samples from CCM were prepared via argon ion cutting using a JEOL IB-19520CCP at 6 kV and room temperature.

26373968, 0, Downloaded from https://onlinelibrary.wiley.com/doi/10.1002/cey2.70300 by Dtsch Zentrum F. Luft-U. Raum Fahrt in D. Helmholtz Gemein., Wiley Online Library on [26/06/2026]. See the Terms and Conditions (https://onlinelibrary.wiley.com/terms-and-conditions) on Wiley Online Library for rules of use; OA articles are governed by the applicable Creative Commons License

For a cross-section of the CL, the samples were prepared by focused ion beam (FIB) at a 54° angle, with angle correction applied for the thickness measurements. Coarse trenches were milled using a 3 nA FIB current at 30 V, and the final surfaces were prepared with a 700 pA FIB current at 30 V. The macro porous area was estimated from SEM images of the CLs using the ImageJ software.

TEM analyses on Pt-e-Cn particles were conducted at 200 kV in HAADF/STEM mode using both FEI THEMIS and Thermo Fischer Spectra 200 microscopes equipped with a Cs probe corrector. For electron energy loss spectroscopy (EELS) measurements, a GIF Continuum device equipped with a K3 camera was used. Samples for TEM analyses were prepared by dispersing Pt-e-Cn powder in water/IPA—simulating the ink formulation (but without ionomer) used for CCM preparation. The resultant dispersion was transferred to TEM grid by drop casting. The average nanoparticle size was determined from TEM images by measuring at least 250 individual particles. The average thickness of the carbon network was determined from over 150 locations across four or more STEM images. It is noted that the TEM grid preparation methods may influence the observed particle size and network thickness; however, this aspect was beyond the scope of the present study.

For MEA cross-section analysis with TEM, a piece of each MEA was first embedded in epoxy resin, and then thin (80–100 nm thick) MEA cross-sections were cut using a LEICA UC6 and a LEICA EM UC7 ultramicrotome. The thin cross sections were deposited on a lacey carbon TEM copper grid for TEM analysis using FEI THEMIS and ThermoFischer Spectra 200 microscopes.

N_2 adsorption-desorption isotherm plots were acquired in a BELSORP-maxII instrument. The surface area of the catalysts was measured using the BET method. The pore size distribution (PSD) was calculated from the desorption branch of the isotherm using the Barrett-Joyner-Halenda (BJH) method. CO displacement measurements on catalyst powder were performed by purging 1% CO in N_2 ($0.25\,L\,min^{-1}$) at 0.55 V, (23 ± 1)°C, 100% RH, and atmospheric pressure in a fuel cell setup. The anode was supplied with $0.25\,L\,min^{-1}$ of 5% H_2 in N_2.

Chemical analyses via XPS were performed using monochromated Al Kα radiation (1486.74 eV) on a spectrometer equipped with a hemispherical electron analyzer and a base pressure of 2×10^{-10} mbar (Thermo Scientific/FEI ESCALAB Xi^+). Signal processing involved the use of convoluted Gaussian/Lorentzian peak profiles and the application of a Shirley background correction [71].

XANES spectra were measured on an easyXAFS 300 + X-ray absorption spectrometer at the Pt L3 edge (11.564 keV, 4.6 eV resolution) using an X-ray source with a Ag anode operating at 30 kV and 24 mA and a Si(911) spherically bent channel-cut monochromator. Samples were prepared by diluting ca. 20 mg of the sample in methyl cellulose to a total weight of 50 mg and pressing into 13 mm pellets of uniform thickness at 10 tons and sealed in Kapton tape. Spectra were collected using a KETEK AXAS-M silicon drift detector with an exposure time for each data point of 30 s. Spectra are the average of 6 scans. Energies were referenced to the known edge energy of Pt foil. The data were analyzed using the Athena and Artemis programs of the Demeter software package [72].

AFM measurements of the electrode surface and the PEM-CL interface were conducted on pristine, activated, and tested CCMs. A $5 \times 5\,mm^2$ sample was cut using a razor blade and affixed to a steel disc covered with conductive carbon tape. To ensure proper electrical contact, an additional piece of conductive tape was placed on the top corner of the sample. AFM measurements were carried out using a Bruker ICON XR AFM. For the CL surface, current mapping over a bias range of 0–2 V (I-V curve) was conducted using DCUBE-TUNA mode, with the bias ramped over a hold time of 0.1 s at each sampling point (128×128 points) within a $100\,\mu m^2$ area. Peak force tapping electronic current measurements (Peak Force TUNA) were conducted to analyze the surface morphology and electronic behavior of the catalyst layer. Electronically conductive areas were estimated quantitatively from AFM electronic conductivity mapping images of the CL surface using the Nanoscope Analysis 3.0 software. For interfacial cross-section measurement between PEM and CL, the Bruker PF-TUNA mode was utilized with NCH-PPT tips (Nanosensors), applying a peak force of 100 nN and an amplitude of 150 nm at a frequency of 0.488 Hz. The CCM cross-sections were prepared by argon ion cutting with a JEOL IB-19520CCP at 6 kV and room temperature. The peak current (i.e., current at maximum force) was used for analysis. Data analysis on AFM images was performed using Nanoscope Analysis 3.0 software.

4.3 | CCM Preparation

The catalyst inks were prepared by dispersing 37.7 mg of catalyst powder in 18 mL of a solvent mixture of water and isopropanol (1:1 volumetric ratio) with 0.26 mL of ionomer solution (Nafion D521, 5 wt.% nafion) using an ultrasonic homogenizer for 45 min at ≈25°C. The final ink concentration was 2.097 mg of powder per ml of ink. The total solid content in the solvent mixture was 0.31%. Nafion NRE 211CS membrane with a thickness of 25 μm was used as the PEM. The relatively thick membrane was selected to minimize gas crossover and endure stable operation during durability testing, albeit at the expense of increased ohmic resistance and associated performance losses. The Pt-e-Cn catalyst produced via FSP and the commercially available Pt/C_{HSA} with ~39 wt.% Pt (Tanaka TEC10E40E) was used as the cathode and anode catalysts, respectively. An in-house optimized ionomer to carbon weight ratio of 0.5 was used for Pt/C_{HSA}. To ensure fair comparison between Pt-e-Cn and Pt/C_{HSA} with different Pt wt.%, the same ionomer to Pt+carbon weight ratio was used for both the inks. An in-house optimized wet spray coating technique was employed for catalyst deposition onto the PEM at 80°C. For comparison, reference CCMs with Pt/C_{HSA} were prepared using the same commercial catalyst (TEC10E40E) on both the anode and cathode sides. A consistent Pt loading of $0.15\,mg\,cm^{-2}$ was achieved for each sample by repeatedly weighing the CCMs before and after catalyst layer deposition, in addition to elemental analysis after deposition. CCMs were used as prepared without hot-pressing. Detailed CCM metrics are provided in Supporting Information S1: Table S8.

26373968, 0, Downloaded from https://onlinelibrary.wiley.com/doi/10.1002/cey2.70300 by Dtsch Zentrum F. Luft-U. Raum Fahrt in D. Helmholtz Gemein., Wiley Online Library on [26/06/2026]. See the Terms and Conditions (https://onlinelibrary.wiley.com/terms-and-conditions) on Wiley Online Library for rules of use; OA articles are governed by the applicable Creative Commons License

4.4 | PEMFC Testing

MEAs with $4 \times 3\ cm^2$ active area were prepared by sandwiching the CCMs between commercial gas diffusion layers (GDL) with a micro-porous layer (MPL) (Sigracet 22 BB, 215 μm thickness) and polyethylene naphthalate gaskets (CMC Klebetechnik). A $12\ cm^2$ differential cell (qCf 12 High Amp) from Baltic fuel cells, in combination with a home-made fuel cell test bench, was used for the experiments. All tests were conducted at 80°C and 80% RH to minimize flooding in the differential cell, unless otherwise specified.

Following cell start-up, the cell was activated in two stages (Supporting Information S1: Table S4). First, the cell was cycled for up to 1000 load cycles in H_2-air by potential cycling between 0.3 and 0.8 V using an anode/cathode stoichiometry of 10 and gas flow rates equivalent to a current density of $3\ A\ cm^{-2}$. Polarization curves were recorded after 100, 500, and 1000 load cycles. Second, a combination of 10 cycles of cathodic CV in H_2-N_2 mode and 50 load cycles in H_2-air mode was performed. CVs were recorded in H_2-N_2 at flow rates of 0.06 and 0.01 $L\ min^{-1}$, with a voltage sweep from 0.1 V to 1.0 V at a scan rate of $50\ mV\ s^{-1}$.

ASTs were performed following the US Department of Energy protocol. Briefly, 30,000 square wave cycles were performed with a 3 s dwell at 0.6 V, a 3 s dwell at 0.95 V, and a 0.5 s ramp between voltage levels, with H_2-N_2 flow rates of 0.07 and 0.02 $L\ min^{-1}$.

Intermediate measurements, including polarization curves, EIS, CV, proton conductivity (PC), and hydrogen cross-over (HCO), were conducted after 0, 100, 1000, 10,000, 20,000, and 30,000 AST cycles. After steady-state operations at 0.5 V for 30 min, the polarization curves were recorded with H_2-air flow rates of 2.508 and 5.998 $L\ min^{-1}$ and back pressures of 150 and 130 kPa_g in potentiostatic mode (Supporting Information S1: Table S9). The used operating conditions in the differential cell are defined in order to mimic the expected local operating conditions at the air inlet of a single cell in a stack working in the EU Harmonized Automotive Reference Operating Conditions for Low Temperature PEMFC at high current density ($2.5\ A/cm^2$; ~0.66 V, $1.65\ W/cm^2$). High current density is chosen to emphasize O_2 transport limitations and anticipate the possible nominal operating point of next-generation MEAs [73]. In contrast to technical small-scale single cells, this approach enables reliable and reproducible characterization of the MEA without impacts, for example, by flooding and local temperature effects. EIS was performed within a frequency range of 50 kHz to 0.1 Hz at current densities of 0.2, 0.5, 1.0, 2.0, and $3.0\ A\ cm^{-2}$, with an AC amplitude of +/−5% of the applied DC current, following a stabilization period of 5 min. Cathodic CV was recorded in H_2-N_2 with flow rates of 0.06 and 0.01 $L\ min^{-1}$, over a voltage range of 0.07 V to 1.0 V at a scan rate of $50\ mV\ s^{-1}$. The measurement was repeated three times to estimate the double-layer capacitance. The ECSA was calculated from the H_{upd} adsorption region, using the lower line of the double-layer capacitance as the baseline. Resistance to proton conduction was measured by performing EIS within a frequency range of 50 kHz to 10 Hz at 0.4 V, with an amplitude of 5 mV, following a stabilization period of 5 min. HCO was determined by applying a constant potential of 0.4 V for 5 min. CO displacement and stripping experiments [12] were conducted on pristine and activated MEAs with Pt-e-Cn and Pt/C_{HSA} electrocatalysts. The cell was conditioned at 40°C with varying relative humidity levels (50%, 60%, 80%, and 100%) and an absolute pressure at anode/cathode of 100/100 kPa. A constant flow ($0.25\ L\ min^{-1}$) of 5% H_2 and 95% N_2 gas mixture was supplied to the anode as a reference, while 100% N_2 was supplied to the cathode for 10 min. Cathode cleaning cycles (10 cycles) were performed by sweeping the voltage from 0.05 V to 1.0 V at a scan rate of $50\ mV\ s^{-1}$, followed by a voltage hold at a predetermined measurement voltage (0.15 V, 0.25 V, 0.35 V, 0.45 V, and 0.55 V) for ≈1 min. CO gas (1% CO in N_2 from Air Liquide) was then introduced to the cathode at $0.25\ L\ min^{-1}$, maintaining the voltage hold for 2 min. Afterward, the cathode was purged with N_2 for 5 min to remove excess CO in the line, before proceeding with CO stripping cyclic voltammetry at a scan rate of $50\ mV\ s^{-1}$. The displacement charge coverage (θ_{dis}) was calculated from the ratio of twice the displacement charge to the stripping charge, as reported by Garrick et al. [12].

Author Contributions

S.V. conceptualized the study. K.A.F., P.G., D.P.E., J.V.H., J.M. acquired funding. S.V., T.M., E.B., D.P.E., L.G., I.B. performed the investigation. S.V., J.M., K.W., P.G. methodology. J.M., P.G., K.A.F. supervised the study. S.V. wrote the original draft. All the authors reviewed and edited the final manuscript.

Acknowledgments

The research leading to these results was supported by the project SUSTAINCELL (Grant Nr. 101101479), which is supported by the Clean Hydrogen Partnership and its members, Hydrogen Europe and Hydrogen Europe Research. We thank the staff of the DLR, Siegfried Graf, Aparna Peethambaran, Noriko Sata, and Martina Gerle for support with fuel cell test bench and FSP operations, and XRD and N_2 adsorption measurements, respectively. We thank the staff of the University of Stuttgart, Florian Kauffmann, for support with the microscopic imaging. Open Access funding enabled and organized by Projekt DEAL.

Disclosure

Co-funded by the European Union. Views and opinions expressed are, however, those of the author(s) only and do not necessarily reflect those of the European Union or the Clean Hydrogen Partnership. Neither the European Union nor the granting authority can be held responsible for them.

Conflicts of Interest

The authors declare no conflicts of interest.

Data Availability Statement

The data that support the findings of this study have been included as part of the electronic supplementary information (ESI). The ESI includes Supporting Information S1: Figures S1–S34 and Supporting Information S1: Tables S1–S9.

References

1. D. Göhl, A. Garg, P. Paciok, et al., "Engineering Stable Electrocatalysts by Synergistic Stabilization Between Carbide Cores and Pt Shells," *Nature Materials* 19, no. 3 (2020): 287–291.

26373968, 0, Downloaded from https://onlinelibrary.wiley.com/doi/10.1002/cey2.70300 by Dtsch Zentrum F. Luft-U. Raum Fahrt in D. Helmholtz Gemein., Wiley Online Library on [26/06/2026]. See the Terms and Conditions (https://onlinelibrary.wiley.com/terms-and-conditions) on Wiley Online Library for rules of use; OA articles are governed by the applicable Creative Commons License

2. X. Ao, L. Li, Y. Ding, et al., "Interatomic Fe-Cu Cooperation in Nitrogen-Doped Carbon for Enhanced Oxygen Reduction," *Energy & Environmental Science* 18, no. 15 (2025): 7624–7634.

3. M. van der Spek, C. Banet, C. Bauer, et al., "Perspective on the Hydrogen Economy as a Pathway to Reach Net-Zero CO_2 Emissions in Europe," *Energy & Environmental Science* 15, no. 3 (2022): 1034–1077.

4. *Strategic Research and Innovation Agenda 2021—2027, Hydrogen End Use: Transport Applications; Clean Hydrogen Joint Undertaking*, published 2022, https://www.clean-hydrogen.europa.eu/knowledge-management/strategy-map-and-key-performance-indicators/clean-hydrogen-ju-sria-key-performance-indicators-kpis_en.

5. K. Kodama, T. Nagai, A. Kuwaki, R. Jinnouchi, and Y. Morimoto, "Challenges in Applying Highly Active Pt-Based Nanostructured Catalysts for Oxygen Reduction Reactions to Fuel Cell Vehicles," *Nature Nanotechnology* 16, no. 2 (2021): 140–147.

6. S. U. S. Satyapal, *DOE Hydrogen Program Annual Merit Review Plenary Remarks*, published 2024, https://www.hydrogen.energy.gov/library/annual-review/2024-annual-merit-review-proceedings.

7. Q. Liu, M. Ranocchiari, and J. A. van Bokhoven, "Catalyst Overcoating Engineering Towards High-Performance Electrocatalysis," *Chemical Society Reviews* 51, no. 1 (2022): 188–236.

8. D. Y. Chung, J. M. Yoo, and Y. E. Sung, "Highly Durable and Active Pt-Based Nanoscale Design for Fuel-Cell Oxygen-Reduction Electrocatalysts," *Advanced Materials* 30, no. 42 (2018): 1704123.

9. J. H. Li, H. Y. Zhang, Q. W. Shi, J. Ying, and C. Janiak, "Encapsulated Pt-Based Nanoparticles for Catalysis," *Progress in Materials Science* 146 (2024): 101335.

10. Tanaka Precious Metals, accessed 2025, https://tanaka-preciousmetals.com/en/products/detail/pefcs/.

11. S. Ott, A. Orfanidi, H. Schmies, et al., "Ionomer Distribution Control in Porous Carbon-Supported Catalyst Layers for High-Power and Low Pt-Loaded Proton Exchange Membrane Fuel Cells," *Nature Materials* 19, no. 1 (2020): 77–85.

12. T. R. Garrick, T. E. Moylan, V. Yarlagadda, and A. Kongkanand, "Characterizing Electrolyte and Platinum Interface in PEM Fuel Cells Using CO Displacement," *Journal of the Electrochemical Society* 164, no. 2 (2017): F60–F64.

13. N. Macauley, R. D. Lousenberg, M. Spinetta, et al., "Highly Durable Fluorinated High Oxygen Permeability Ionomers for Proton Exchange Membrane Fuel Cells," *Advanced Energy Materials* 12, no. 45 (2022): 2201063.

14. *Strategic Research and Innovation Agenda 2021—2027, Annex 4—State-of-the-art and Future Targets—Hydrogen End Use: Transport Applications, KPIs for Fuel Cell Technology for Heavy-Duty-Vehicles Clean Hydrogen Joint Undertaking*, (2022): 163–165, https://www.horizon-europe.gouv.fr/sites/default/files/2022-03/programme-strat-gique-de-recherche-et-d-innovation-de-clean-hydrogen-5867.pdf.

15. K. Guo, L. Bao, Z. Yu, and X. Lu, "Carbon Encapsulated Nanoparticles: Materials Science and Energy Applications," *Chemical Society Reviews* 53, no. 22 (2024): 11100–11164.

16. S. Shin, E. Lee, J. Nam, et al., "Carbon-Embedded Pt Alloy Cluster Catalysts for Proton Exchange Membrane Fuel Cells," *Advanced Energy Materials* 14, no. 29 (2024): 2400599.

17. S. Venkatesan, J. Mitzel, K. Wegner, R. Costa, P. Gazdzicki, and K. A. Friedrich, "Nanomaterials and Films for Polymer Electrolyte Membrane Fuel Cells and Solid Oxide Cells by Flame Spray Pyrolysis," *Renewable and Sustainable Energy Reviews* 158 (2022): 112080.

18. S. Venkatesan, J. Mitzel, S. S. Ambu, et al., "Rapid Scalable One-Step Production of Catalysts for Low-Iridium Content Proton Exchange Membrane Water Electrolyzers," *Advanced Energy Materials* (2024): 2401659.

19. L. Mädler, H. K. Kammler, R. Mueller, and S. E. Pratsinis, "Controlled Synthesis of Nanostructured Particles by Flame Spray Pyrolysis," *Journal of Aerosol Science* 33, no. 2 (2002): 369–389.

20. S. Venkatesan, J. Mitzel, S. S. Ambu, et al., "Rapid Scalable One-Step Production of Catalysts for Low-Iridium Content Proton Exchange Membrane Water Electrolyzers," *Advanced Energy Materials* 15, no. 1 (2025): 2570004.

21. S. Pokhrel, J. Stahl, J. D. Groeneveld, et al., "Flame Aerosol Synthesis of Metal Sulfides at High Temperature in Oxygen-Lean Atmosphere," *Advanced Materials* 35, no. 28 (2023): 2211104.

22. V. Muravev, A. Parastaev, Y. van den Bosch, et al., "Size of Cerium Dioxide Support Nanocrystals Dictates Reactivity of Highly Dispersed Palladium Catalysts," *Science* 380, no. 6650 (2023): 1174–1179.

23. S. Liu, C. Dun, J. Chen, et al., "A General Route to Flame Aerosol Synthesis and In Situ Functionalization of Mesoporous Silica," *Angewandte Chemie International Edition* 61, no. 35 (2022): e202206870.

24. F. O. Ernst, R. Büchel, R. Strobel, and S. E. Pratsinis, "One-Step Flame-Synthesis of Carbon-Embedded and -Supported Platinum Clusters," *Chemistry of Materials* 20, no. 6 (2008): 2117–2123.

25. R. Koirala, S. E. Pratsinis, and A. Baiker, "Synthesis of Catalytic Materials in Flames: Opportunities and Challenges," *Chemical Society Reviews* 45, no. 11 (2016): 3053–3068.

26. B. Schimmoeller, S. E. Pratsinis, and A. Baiker, "Flame Aerosol Synthesis of Metal Oxide Catalysts With Unprecedented Structural and Catalytic Properties," *ChemCatChem* 3, no. 8 (2011): 1234–1256.

27. K. Wegner, B. Schimmöller, B. Thiebaut, C. Fernandez, and T. N. Rao, "Pilot Plants for Industrial Nanoparticle Production by Flame Spray Pyrolysis," *Kona Powder and Particle Journal* 29, no. 2011 (2011): 251–265.

28. B. Fang, L. Daniel, A. Bonakdarpour, R. Govindarajan, J. Sharman, and D. P. Wilkinson, "Dense Pt Nanowire Electrocatalyst for Improved Fuel Cell Performance Using a Graphitic Carbon Nitride-Decorated Hierarchical Nanocarbon Support," *Small* 17, no. 30 (2021): 2102288.

29. T. H. Fleisch, G. W. Zajac, J. O. Schreiner, and G. J. Mains, "An XPS Study of the UV Photoreduction of Transition and Noble-Metal Oxides," *Applied Surface Science* 26, no. 4 (1986): 488–497.

30. L. A. da Silva, V. A. Alves, S. C. de Castro, and J. F. C. Boodts, "XPS Study of the State of Iridium, Platinum, Titanium and Oxygen in Thermally Formed IrO+TiO+PtO Films," *Colloid Surface* A170, no. 2–3 (2000): 19–126.

31. Y. Zhang, M. L. Toebes, A. van der Eerden, W. E. O'Grady, K. P. de Jong, and D. C. Koningsberger, "Metal Particle Size and Structure of the Metal-Support Interface of Carbon-Supported Platinum Catalysts as Determined With EXAFS Spectroscopy," *Journal of Physical Chemistry B* 108, no. 48 (2004): 18509–18519.

32. α-PtO_2 (PtO_2 rt) Crystal Structure, SpringerMaterials (online database), accessed November 11, 2025, https://materials.springer.com/isp/crystallographic/docs/sd_1123350.

33. R. K. Nomiyama, M. J. Piotrowski, and J. L. F. Da Silva, "Bulk Structures of PtO and PtO_2 From Density Functional Calculations," *Physical Review* B 84, no. 10 (2011): 100101.

34. J. Yang and F. Gao, "First Principles Calculations of Mechanical Properties of Cubic 5d Transition Metal Monocarbides," *Physica B: Condensed Matter* 407, no. 17 (2012): 3527–3534.

35. T. Cui, L. Ma, S. Wang, et al., "Atomically Dispersed Pt-N_3C_1 Sites Enabling Efficient and Selective Electrocatalytic C-C Bond Cleavage in Lignin Models Under Ambient Conditions," *Journal of the American Chemical Society* 143, no. 25 (2021): 9429–9439.

36. A. Reinholdt and J. Bendix, "Platinum(II) as An Assembly Point for Carbide and Nitride Ligands," *Chemical Communications* 55, no. 57 (2019): 8270–8273.

26373368, 0, Downloaded from https://onlinelibrary.wiley.com/doi/10.1002/cey2.70300 by Dtsch Zentrum F. Luft-U. Raum Fahrt in D. Helmholtz Gemein., Wiley Online Library on [26/06/2026]. See the Terms and Conditions (https://onlinelibrary.wiley.com/terms-and-conditions) on Wiley Online Library for rules of use; OA articles are governed by the applicable Creative Commons License

37. V. P. Babar, S. Jaiswal, and V. Kumar, "Interaction of a Carbon Atom on Small Platinum Clusters and Its Effects on Hydrogen Binding," *Chemical Physics Letters* 560 (2013): 42–48.

38. R. Zhang, L. Song, and Y. Wang, "Insight Into the Adsorption and Dissociation of CH_4 on Pt(*hkl*) Surfaces: A Theoretical Study," *Applied Surface Science* 258, no. 18 (2012): 7154–7160.

39. S. K. Friedlander, *Smoke, Dust, and Haze: Fundamentals of Aerosol Dynamics* (Oxford University Press, 2000).

40. H. Lee, T. J. Kim, C. Li, et al., "Flame Aerosol Synthesis of Carbon-Supported Pt-Ru Catalysts for a Fuel Cell Electrode," *International Journal of Hydrogen Energy* 39, no. 26 (2014): 14416–14420.

41. S. Stariha, N. Macauley, B. T. Sneed, et al., "Recent Advances in Catalyst Accelerated Stress Tests for Polymer Electrolyte Membrane Fuel Cells," *Journal of the Electrochemical Society* 165, no. 7 (2018): F492–F501.

42. T. Y. Yoo, J. Lee, S. Kim, et al., "Scalable Production of an Intermetallic Pt-Co Electrocatalyst for High-Power Proton-Exchange-Membrane Fuel Cells," *Energy & Environmental Science* 16, no. 3 (2023): 1146–1154.

43. Z. Zhao, Z. Liu, A. Zhang, et al., "Graphene-Nanopocket-Encaged PtCo Nanocatalysts for Highly Durable Fuel Cell Operation Under Demanding Ultralow-Pt-Loading Conditions," *Nature Nanotechnology* 17, no. 9 (2022): 968–975.

44. B. Peng, Z. Liu, L. Sementa, et al., "Embedded Oxide Clusters Stabilize sub-2 nm Pt Nanoparticles for Highly Durable Fuel Cells," *Nature Catalysis* 7, no. 7 (2024): 818–828.

45. J. Liang, H. Yu, M. J. Zachman, et al., "Creating Favorable Pt/Co Interfaces via a Two-Step Approach for Constructing Highly Durable PtCo Intermetallic Fuel Cell Catalysts," *Advanced Materials* 38, no. 7 (2025): e10847.

46. T. W. Song, J. J. Yan, L. Tong, et al., "Core/Shell-Structured Carbon Support Boosting Fuel Cell Durability," *Advanced Materials* 37, no. 17 (2025): 2414472.

47. Y. Zeng, J. Liang, C. Li, et al., "Regulating Catalytic Properties and Thermal Stability of Pt and PtCo Intermetallic Fuel-Cell Catalysts via Strong Coupling Effects Between Single-Metal Site-Rich Carbon and Pt," *Journal of the American Chemical Society* 145, no. 32 (2023): 17643–17655.

48. M. Karuppannan, Y. Kim, S. Gok, et al., "A Highly Durable Carbon-Nanofiber-Supported Pt-C Core-Shell Cathode Catalyst for Ultra-Low Pt Loading Proton Exchange Membrane Fuel Cells: Facile Carbon Encapsulation," *Energy & Environmental Science* 12, no. 9 (2019): 2820–2829.

49. X. Hu, K. Jiang, F. Wang, et al., "Gas Dynamically Confined Synthesis of Platinum-Based Intermetallic Nanowires for Active and Ultrastable Oxygen Reduction Catalysis," *ACS Nano* 19, no. 34 (2025): 31201–31212.

50. X. Liu, Y. Wang, J. Liang, et al., "Introducing Electron Buffers into Intermetallic Pt Alloys Against Surface Polarization for High-Performing Fuel Cells," *Journal of the American Chemical Society* 146, no. 3 (2024): 2033–2042.

51. E. Lee, H. Jin, H. Jo, et al., "Suppressing Metal Dissolution in Multi-Grained Catalysts Through Intragrain Atomic Ordering for Stable Fuel Cells," *Advanced Materials* 37, no. 35 (2025): 2504059.

52. C. Gyan-Barimah, J. S. P. Mantha, H. Y. Lee, et al., "High Vacancy Formation Energy Boosts the Stability of Structurally Ordered PtMg in Hydrogen Fuel Cells," *Nature Communications* 15, no. 1 (2024): 7034.

53. Z. Qiao, C. Wang, C. Li, et al., "Atomically Dispersed Single Iron Sites for Promoting Pt and Pt_3Co Fuel Cell Catalysts: Performance and Durability Improvements," *Energy & Environmental Science* 14, no. 9 (2021): 4948–4960.

54. Q. Cheng, S. Yang, C. Fu, et al., "High-Loaded sub-6 nm Pt_1Co_1 Intermetallic Compounds With Highly Efficient Performance Expression in PEMFCs," *Energy & Environmental Science* 15, no. 1 (2022): 278–286.

55. Z. Li, J. Zou, X. Xi, et al., "Native Ligand Carbonization Renders Common Platinum Nanoparticles Highly Durable for Electrocatalytic Oxygen Reduction: Annealing Temperature Matters," *Advanced Materials* 34, no. 26 (2022): 2202743.

56. J. Liang, Y. Wan, H. Lv, et al., "Metal Bond Strength Regulation Enables Large-Scale Synthesis of Intermetallic Nanocrystals for Practical Fuel Cells," *Nature Materials* 23, no. 9 (2024): 1259–1267.

57. Y. Ma, J. Peng, J. Tian, et al., "Highly Stable and Active Catalyst in Fuel Cells Through Surface Atomic Ordering," *Science Advances* 10, no. 42 (2024): eado4935.

58. S. N. Hu, W. C. Xu, N. Tian, et al., "A P-O Functional Group Anchoring Pt-Co Electrocatalyst for High-Durability PEMFCs," *Energy & Environmental Science* 17, no. 9 (2024): 3099–3111.

59. D. Li, C. Wang, D. S. Strmcnik, et al., "Functional Links Between Pt Single Crystal Morphology and Nanoparticles With Different Size and Shape: The Oxygen Reduction Reaction Case," *Energy & Environmental Science* 7, no. 12 (2014): 4061–4069.

60. D. J. S. Sandbeck, O. Brummel, K. J. J. Mayrhofer, J. Libuda, I. Katsounaros, and S. Cherevko, "Dissolution of Platinum Single Crystals in Acidic Medium," *Chemphyschem* 20, no. 22 (2019): 2997–3003.

61. S. Wang, E. Zhu, Y. Huang, and H. Heinz, "Direct Correlation of Oxygen Adsorption on Platinum-Electrolyte Interfaces With the Activity in the Oxygen Reduction Reaction," *Science Advances* 7, no. 24 (2021): eabb1435.

62. H. Tanaka, Y. Nagahara, S. Sugawara, K. Shinohara, M. Nakamura, and N. Hoshi, "The Influence of Pt Oxide Film on the Activity for the Oxygen Reduction Reaction on Pt Single Crystal Electrodes," *Electrocatalysis* 5, no. 4 (2014): 354–360.

63. K. Nagamori, S. Aoki, M. Ikegawa, et al., "Impacts of Pt/Carbon Black Catalyst Surface Hydrophilicity on Ionomer Distribution and Durability During Water-Generating Load Cycling of Polymer Electrolyte Fuel Cells," *ACS Applied Energy Materials* 6, no. 22 (2023): 11481–11496.

64. S. Arisetty, X. Wang, R. K. Ahluwalia, et al., "Catalyst Durability in PEM Fuel Cells With Low Platinum Loading," *Journal of the Electrochemical Society* 159, no. 5 (2012): B455–B462.

65. K. Shinozaki, H. Yamada, and Y. Morimoto, "Relative Humidity Dependence of Pt Utilization in Polymer Electrolyte Fuel Cell Electrodes: Effects of Electrode Thickness, Ionomer-to-Carbon Ratio, Ionomer Equivalent Weight, and Carbon Support," *Journal of the Electrochemical Society* 158, no. 5 (2011): B467–B475.

66. A. Perego, A. Avid, D. N. Mamania, et al., "Investigation of Cathode Catalyst Layer Interfaces Evolution During Accelerated Stress Tests for Polymer Electrolyte Fuel Cells," *Applied Catalysis, B: Environmental* 301 (2022): 120810.

67. X. Li, F. Tang, Q. Wang, et al., "Modeling of Local Mass Transport in Cathode Catalyst Layer of Proton Exchange Membrane Fuel Cell: Catalyst Partially Covered by Ionomer," *International Journal of Hydrogen Energy* 50 (2024): 1228–1238.

68. J. Liu and I. V. Zenyuk, "Proton Transport in Ionomer-Free Regions of Polymer Electrolyte Fuel Cells and Implications for Oxygen Reduction Reaction," *Current Opinion in Electrochemistry* 12 (2018): 202–208.

69. E. Padgett, V. Yarlagadda, M. E. Holtz, et al., "Mitigation of PEM Fuel Cell Catalyst Degradation With Porous Carbon Supports," *Journal of the Electrochemical Society* 166, no. 4 (2019): F198–F207.

26373968, 0, Downloaded from https://onlinelibrary.wiley.com/doi/10.1002/cey2.70300 by Dtsch Zentrum F. Luft-U. Raum Fahrt in D. Helmholtz Gemein., Wiley Online Library on [26/06/2026]. See the Terms and Conditions (https://onlinelibrary.wiley.com/terms-and-conditions) on Wiley Online Library for rules of use; OA articles are governed by the applicable Creative Commons License

70. D. Schonvogel, N. K. Nagappan, J. Müller-Hülstede, N. Bengen, and P. Wagner, "Effect of Fe-N-Cs as Catalytic Active Support for Platinum Towards ORR in Acidic Environment," *Journal of the Electrochemical Society* 170, no. 11 (2023): 114518.

71. R. Hesse, T. Chassé, and R. Szargan, "Peak Shape Analysis of Core Level Photoelectron Spectra Using UNIFIT for WINDOWS," *Fresenius' Journal of Analytical Chemistry* 365, no. 1/3 (1999): 48–54.

72. B. Ravel and M. Newville, "Athena, Artemis, Hephaestus: Data Analysis for X-Ray Absorption Spectroscopy Using FEFFIT," *Journal of Synchrotron Radiation* 12 (2005): 537–541.

73. G. Tsotridis, A. Pilenga, G. D. Marco, and T. Malkow, *EU Harmonized Test Protocols for PEMFC MEA Testing in Single Cell Configuration for Automotive Applications* (Publications Office of the European Union, 2016), JRC99115, https://doi.org/10.2790/54653. https://publications.jrc.ec.europa.eu/repository/handle/JRC99115.

Supporting Information

Additional supporting information can be found online in the Supporting Information section.

Supporting File: cey270300-sup-0001-Venkatesan-et_al_Supplemental-information.pdf.

26373938, 0, Downloaded from https://onlinelibrary.wiley.com/doi/10.1002/cey2.70300 by Dtsch Zentrum F. Luft-U. Raum Fahrt in D. Helmholtz Gemein., Wiley Online Library on [26/06/2026]. See the Terms and Conditions (https://onlinelibrary.wiley.com/terms-and-conditions) on Wiley Online Library for rules of use; OA articles are governed by the applicable Creative Commons License